Paper 143

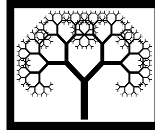

©Civil-Comp Press, 2012
Proceedings of the Eleventh International Conference
on Computational Structures Technology,
B.H.V. Topping, (Editor),
Civil-Comp Press, Stirlingshire, Scotland

On the Modelling of the Direct Bonding of Two Silicon Surfaces

N. Cocheteau[1], F. Lebon[1], I. Rosu[1], A. Maurel[1]
S. AitZaid[2] and I. Savin DeLarclause[2]
[1] Laboratory of Mechanic and Acoustics, University of Aix-Marseille, France
[2] National Centre for Spatial Studies, Toulouse, France

Abstract

Direct bonding is a process that does not require the use of any adhesive material. This process is based on short-range interatomic attraction forces such as hydrogen bonds. In this paper, chemical analyses and mechanical tests were performed in order to characterize silicon surfaces and the mechanical resistance of the bonded interfaces formed by these surfaces. Various methods of modelling adhesive contacts in order to predict the mechanical resistance of these assemblies are then compared.

Keywords: silicon direct bonding, modelling, finite elements, surface energy, roughness, mechanical tests.

1 Introduction

Direct bonding consists in joining two surfaces without using any adhesives or other additional materials [1], usually by bringing two flat, well-polished surfaces into contact at room temperature, which causes them to adhere spontaneously to each other. Once the bonding process has been initiated, it will spread along the whole interface. At the macroscopic scale, no gap can be observed at the interface thus formed because the two bodies are only an atomic distance apart. The attraction forces responsible for this process are van der Waals forces or hydrogen bonds. The three main parameters involved are the deformability of the material, the surface energy of adhesion and the surface roughness [2].
Direct bonding processes were first applied in the field of microelectronics, to produce bonded silicon on insulator (SOI) wafers and electronic substrates, for example. These processes are also being used in epitaxial applications [3, 4]. They are of particular interest to manufacturers of spatial instruments such as interferometers, slicers, etc. Advantages such as the high-precision production processes involved and the dimensional stability of the assemblies obtained are due

to the fact that no mechanical parts or glue are required. In addition, since no adhesive materials are used in these processes, the risks of contamination associated with degassing are avoided. These glueless methods are also environmentally friendly, since industrial glue production causes chemical pollution. However, this bonding process is poorly reproducible. In addition, the constraints involved in spatial applications (thermal fatigue, vibrations, etc.) are very different from those encountered on Earth. To be applicable in spatial contexts, this technology needs better process control and greater reproducibility, and the mechanical performances of adhesive bonds need to be improved without detracting from the optical characteristics of the materials used. The aim of this study was therefore to compare the various ways of modelling this particular type of adhesive contact in the framework of finite elements methods. Classical models, such as the virtual crack closure technique and cohesive elements models, and models in which adhesion is combined with cohesive elements are therefore compared.
The direct bonding process is presented in Section 2. Methods of characterizing, chemical surfaces are discussed in Section 3 and mechanical tests for characterizing the mechanical resistance of bonded interfaces are reviewed in Section 4. Various adhesion models and the results of the first simulations performed using these models are presented and discussed in Section 5.

2 Hydrophilic direct bonding

As explained above, silicon direct bonding consists in joining two surfaces without using any adhesives. The surfaces to which molecular bonding processes can be applied are of two kinds: hydrophilic and hydrophobic surfaces. The main difference between these two types of surfaces focuses on the thin film of water present on hydrophilic surfaces, corresponding to the molecular layers adsorbed during the bonding process.

2.1 Preparation of the surfaces

Direct bonding is possible as long as the two surfaces are very similar. The first step in the bonding process therefore consists in polishing them several times in order to obtain the exact surface roughness, flatness and deflection required [5].
A chemical treatment is then required in order to eliminate any contaminating particles: a particle as small as 0.5 µm in diameter can cause a bonding defect 2.5mm in diameter. This treatment also activates the surfaces in order to make them hydrophilic or hydrophobic, as required.

2.2 Silicon direct bonding at room temperature

Once the surface treatment has been completed, bonding occurs between the saturated terminal hydroxyl groups of the two surfaces. A process of capillarity occurs due to the humid air trapped between the surfaces [6]. When a slight local

pressure is applied, the surfaces are brought closer together, and hydrogen bonds develop between the water molecules and the two surfaces at this pressure application point (Figure 1) [7]. These hydrogen bonds attract the two surfaces until the equilibrium distance between the bonds is reached. When the surfaces move closer, other hydrogen bonds develop which bring the surfaces even closer together, as shown in Figure 1. A bonding wave propagates from the contact point through the whole sample, resulting in the bonding of the surfaces. Water molecules migrate from the bonding interface and/or diffuse at the interface, bringing the surfaces even closer together and initiating silanol-silanol interactions (Figure 1 and 2) [7-10].

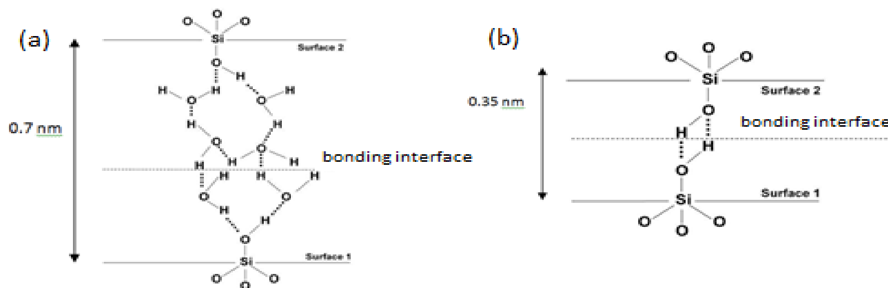

Figure 1: Chemical structure of an interface after two hydrophilic surfaces have been brought into contact (a) and after water evacuation (b).

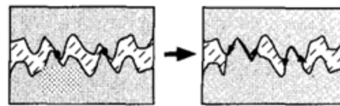

Figure 2: Microscopic view of the closure of an interface due to the enlargement of the contact point.

However, this sealing process is reversible [11]. In order to obtain a stronger or irreversible seal by increasing the number of covalent bonds, it is necessary to change the nature of the bonds at the interface by applying a thermal treatment (Figure 3, Figure 4).

- Between 25°C and 200°C, the water molecules diffuse and silanol interactions are initiated.
- Between 200°C and 700°C, the chemical bonds are rearranged and form strong hydrogen bonds. A polymerization reaction is triggered, resulting in the formation of covalent siloxane bonds (Figure 3)
- Up to 700°C, increasing numbers of covalent siloxane bonds are formed and the bonding energy is enhanced [6].

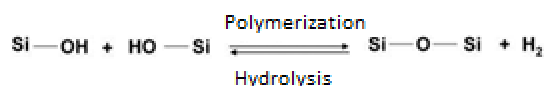

Figure 3: Polymerization reaction.

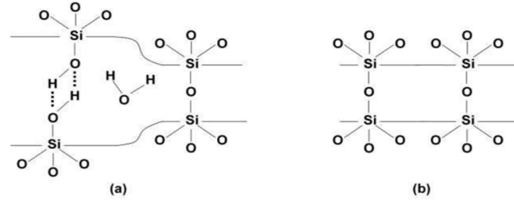

Figure 4: Evolution of a bonding interface (a) during thermal treatment (b) after a long treatment.

3 Chemical characterization of surfaces

In this section, some data on the chemical surfaces of two materials, silicon glass and Zerodur®, are presented. Surface wettability, X-ray photoelectron spectroscopy (XPS), roughness and flatness measurements were performed in order to characterize these glassy surfaces. Chemical analyses were performed on surfaces of two kinds: non-bonded surfaces and debonded surfaces.
Drops of various liquids were deposited on the surface in order to determine the surface energy of the solids under investigation by measuring the drop angle (Table 1) [12].

$$\boldsymbol{\gamma_s = \gamma_{sl} + \gamma_l . \cos\theta} \tag{1}$$

where γs and γ_l are the surface tension of the solid and liquid, respectively. γ_{sl} is the liquid/solid interfacial tension and θ is the contact angle**.** Since the surface energy γ_{sl} cannot be measure directly, the Owen Wendt model is used:

$$\gamma_l . (1 + \cos\theta) = 2.\sqrt{\gamma_s^p \gamma_l^p} + 2.\sqrt{\gamma_s^d \gamma_l^d} \tag{2}$$

where $\gamma_{s,}^p$ and γ_l^p are the polar components and $\gamma_{s,}^d$ and γ_l^d are the dispersive component of γs and γ_l respectively.
The drop angle was measured using a special device consisting of a camera and a light source. The angle was determined by approximating the drop profile using the Drop Shape Analysis v.1.80 software program [13]. The drop volume used here for this purpose was 1µL in size.

liquids	γ_l [mN/m]	γ_l^d [mN/m]	γ_l^p [mN/m]
Benzyl alcohol	39.00	30.30	8.70
Glycol ethylene	47.70	26.40	21.30
Deionised water	72.80	26.00	46.80
Diiodo-methane	50.80	50.80	0.00

Table 1: Liquids used for surface wettability tests.

Samples	γ_s	γ_s^d	γ_s^p
	mJ/m²	mJ/m²	mJ/m²
1-A-M-1 Zerodur	**51,59**	27,69	23,91
	51,56	28,15	23,42
1-A-M-2 Zerodur	**46,61**	29,2	17,41
	49,3	29,88	19,42
1-A-M-3 Silicon	**48,57**	29,49	19,19
	53,11	28,48	24,63
1-A-M-4 Zerodur (debond)	**40,43**	23,96	16,48
	43,26	25,74	17,51
1-A-M-5 Silicon (debond)	**41,52**	26,11	15,41
	38,76	26,79	12,02

Table 2: Surface wettability results.

The surface energy of the Zerodur® samples is greater than that of silicon samples (Table 2). The difference in surface energy between non-bonded and debonded surfaces was found to be approximately 20%. The results of the XPS tests presented in Figure 5 show that the spectra of debonded and non-bonded surfaces were identical *a priori*. The differences between silicon and Zerodur® are attributable to the differences in the chemical composition of the two materials. Since the silica atoms do not have the same environment in both cases, the oxidation rates differ.
Based on the surface wettability and XPS data obtained, this process can be said to be chemically reversible.

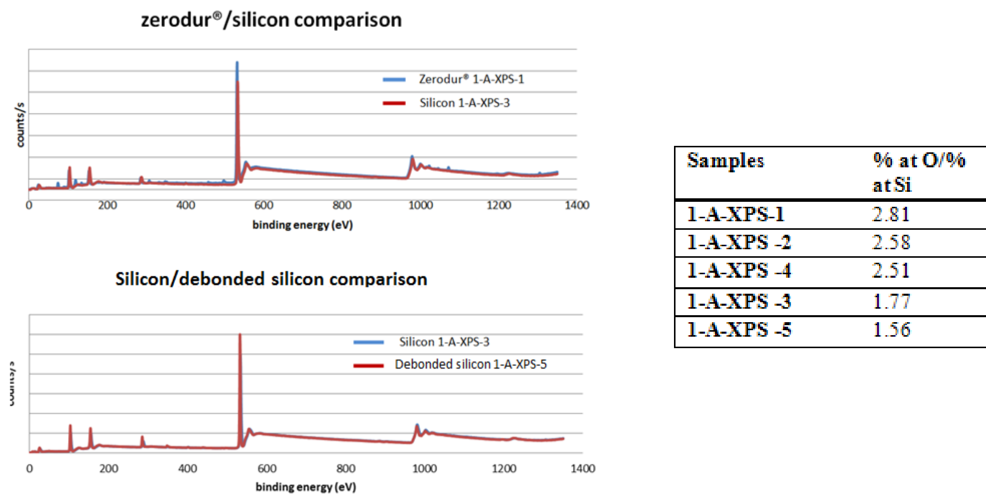

Samples	% at O/% at Si
1-A-XPS-1	2.81
1-A-XPS -2	2.58
1-A-XPS -4	2.51
1-A-XPS -3	1.77
1-A-XPS -5	1.56

Figure 5: XPS spectra and atomic oxygen rates on Zerodur® and silicon samples.

The characteristics of the surfaces are presented in Appendix A. Roughness and flatness was measured with the ZYGO GPI and ZYGO NIEW VIEW devices [14-15]. A light beam 0.5 mm² in diameter was projected onto the surface and the fringe interferences obtained gave the roughness and flatness values.

4 Mechanical tests

In this section, the results of some mechanical experiments are presented. Double shear tests and double cantilever beam tests were performed to determine the bonding energy of the interface and the influence of thermal treatment on the mechanical resistance of the assemblies.

4.1 Double shear test

The samples tested each consisted of three bonded cylindrical Silicon and Zerodur® parts, which were annealed for 15h under nitrogen atmosphere, as shown in Figure 6. Five samples were annealed concomitantly in order to check the possible existence of a thermal gradient in the furnace. The results showed that no thermal gradient was present.
With the Zerodur® samples, we had to work at temperatures below 550°C in order to preserve properties such as the thermal expansion coefficient.

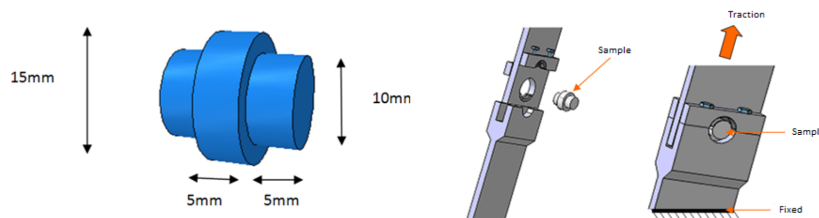

Figure 6: Sample and assembly for double shear stress tests.

As shown in Figure 7 the mechanical resistance of the samples was found to increase non linearly with the temperature. The optimum temperature for testing silicon and Zerodur® samples was found to be 800°C and 400°C, respectively.
Bonded Zerodur® interfaces are also more resistant than bonded silicon interfaces [16].

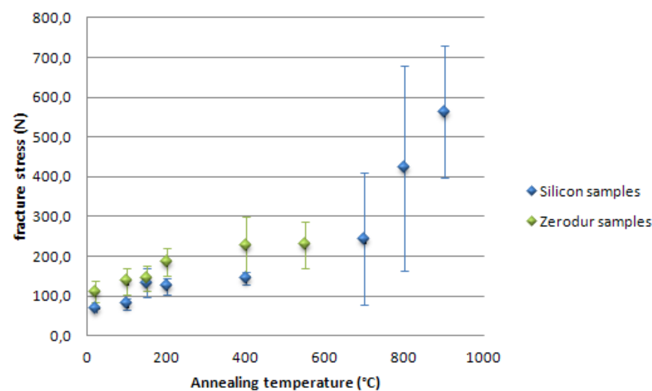

Figure 7: Results of double shear stress tests: comparison between silicon and Zerodur samples.

However, the results obtained showed considerable dispersion, possibly because of the thermal treatment and/or the mechanical test procedure used.

4.2 Double cantilever beam tests

One of the main parameters generally used to characterize adhesion is the bonding energy. The adhesion can be quantified in term of the Dupré work of adhesion or adhesion force [17]. In the case of brittle material, the work of adhesion can be measured using fracture mechanics theory.
The work of adhesion is related to the surface energies in equation (3).

$$\mathbf{W_{adhesion}} = \boldsymbol{\gamma_1} + \boldsymbol{\gamma_2} - \boldsymbol{\gamma_{12}} \tag{3}$$

where γ_{12} is the interface energy [18]. γ_1 and γ_2 were measured by performing the surface wettability tests presented in Section 3. Here $\gamma_1 = \gamma_2 = \gamma_s$.

The most popular method of measuring the bonding energy $\boldsymbol{\gamma_{12}}$ is the crack propagation method, which is also known as the razor blade method, Maszara test or double cantilever beam test.
As shown in Figure 8, a razor blade is inserted at the interface, causing the two silicon glass wafers to curve and a crack to develop. This crack propagates along the interface until equilibrium is reached between the elastic forces and the hydrogen bonds responsible for the adhesion. At equilibrium, the critical strain energy release rate G_{1C} is equal to the work of adhesion [19].

$$\mathbf{W_{adhesion}} = \mathbf{G_{1C}} \tag{4}$$

The length L of the debonded crack reflects the G_{1C} , and hence the interface energy. This parameter can be measured via the infrared transparency of the silicon glass and the contrast with air [20-22].

As established by Maszara and Al. [23] the G_{1C} can be related to the length L using the following equation (5).

$$\mathbf{G_{1C}} = \frac{3y^2 E_1' t_1^3 E_2' t_2^3}{16L^4 (E_1' t_1^3 + E_2' t_2^3)} \tag{5}$$

where $E' = \frac{E}{1-\upsilon^2}$, t_1 and t_2 are the thickness of the two surfaces, y is the thickness of the razor blade, E_1 and E_2 are the Young's modulus , ν_1 and ν_2 are the Poisson's ratio.

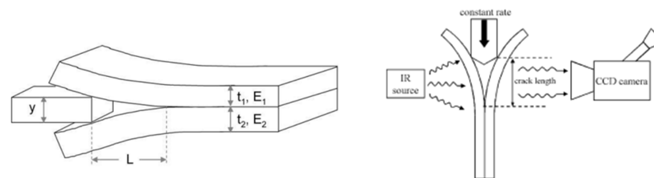

Figure 8: Razor blade methods.

5 Double cantilever beam modelling

In this section, some appropriate models are presented. The main parameters used in these models are the Young's modulus ($N.m^{-2}$), the specific surface energy of adhesion ($N.m^{-1}$) and the roughness of the two surfaces. The roughness can be characterized by the height h of the asperities and the wavelength L (Figure 9).
A high level of roughness results in a weak contact zone and thus in the occurrence of defects during the bonding process. When the roughness is too great, bonding becomes impossible. The bonding will obviously be easier to perform when the surface energy of adhesion is high, the Young's modulus is low and the surfaces are smooth, giving high wavelength values [24, 25].
It is proposed here to compare various methods of modelling adhesive contacts, or more specifically, models for the debonding occurring in the presence of an external force.
The first model is based on the virtual crack closure technique and the second one is based on the cohesive elements approach.

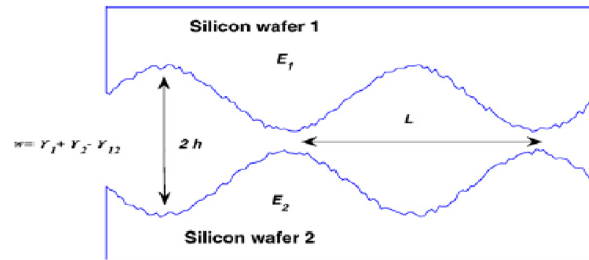

Figure 9: Cross section of two silicon glass samples bonded by molecular adhesion.

5.1 Theoretical models

5.1.1 The virtual crack closure technique (VCCT) model

In the first model, the virtual crack closure technique (VCCT), which is based on linear elastic fracture mechanics, is used to predict the crack propagation process occurring along a predefined surface. The strain energy released when a crack is extended by a given amount is assumed here to be the same as the energy required to close the crack by the same amount. The fracture process is initiated at any given node under mixed mode condition when the equivalent strain energy release rate G_{equiv} calculated at that node is greater than the critical equivalent strain energy rate G_{equivc} calculated on the basis of a specific mixed mode criterion. One such criterion is the power law (6) [21-24].

$$\mathbf{G_{equiv}} = \left(\frac{\mathbf{G_I}}{\mathbf{G_{IC}}}\right)^{\mathbf{am}} + \left(\frac{\mathbf{G_{II}}}{\mathbf{G_{IIC}}}\right)^{\mathbf{an}} + \left(\frac{\mathbf{G_{III}}}{\mathbf{G_{IIIC}}}\right)^{\mathbf{ao}} \quad (6)$$

where G_{IC}, G_{IIC} and G_{IIIC} are the critical energy release rates associated with pure modes I, II and III, respectively and am, an, and ao are three parameters associated with these three modes.
The other two criteria which can be used to calculate the equivalent strain energy release rate are the Reeder law and the BK law [29].

5.1.2 Cohesive element modelling methods

Cohesive elements methods are used to model bonded interfaces in which the thickness is negligible. These methods focus on the initial loading, the initiation of damage and the propagation of the damage.
A traction-separation based constitutive response is defined by an adhesive material.
A commonly used traction-separation law is presented in Figure 10.

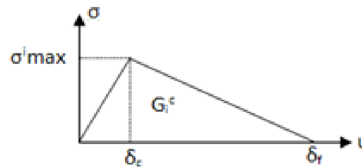

Figure 10: Traction-separation law used to define cohesive elements.

Damage initiation refers to the onset of the degradation of the response of a material point as the result of the stress and/or the strain. Under mixed mode loading conditions, the quadratic nominal stress criterion defined by equation (7) is used to simulate the onset of the damage. When this ratio reaches the yield value, damage is initiated.

$$\left\{\frac{\langle\sigma_n\rangle}{\sigma_n^0}\right\}^2 + \left\{\frac{\sigma_s}{\sigma_s^0}\right\}^2 + \left\{\frac{\sigma_t}{\sigma_t^0}\right\}^2 = 1 \quad (7)$$

where $\sigma_n^0, \sigma_s^0, \sigma_t^0$ denote the maximum stress ratio and $\sigma_n, \sigma_s, \sigma_t$ denote the nominal stress ratio in the purely normal mode, the first shear direction and the second shear direction, respectively. The damage evolution is defined as the rate at which the stiffness of the material is degraded as from the moment at which the corresponding initiation criterion is reached. Damage evolution is defined by the fracture energy. Components of the fracture energies associated with each fracture mode have to be specified as properties of the material in the same way as the VCCT criteria. For example, the expression for the power law given in (6) can be used to express the damage evolution [26, 29].

5.1.3 Modelling the surface characteristics using cohesive elements

One of the advantages of using cohesive element models is that the users can define their own traction-separation law.
Since the roughness is one of the main parameters involved, it has to be taken into account. Two bonded nodes (each of which corresponds to a surface area of 0.5mm², the cell size of a roughness measurement) – one in each surface – will debond when

the external force imposed on these nodes reaches a predefined force. The predefined force at each node can be calculated by adding together the forces acting on each asperity in a surface area of 0.5 mm². This force can be determined using two physical models taking the surface energy of adhesion and roughness into account.
The model based on the roughness of two surfaces with the original distribution height h_i is equivalent to the model assuming that one of the contact surfaces (the lower one) is perfectly rigid and flat and not deformed in the contact, and that the other one (the higher one) has a combined height distribution (Figure 11). The solid line in figure 11 stands for the silicon contact interface before bonding and the dashed line stands for the interface during the bonding. Only h_i can be measured by performing roughness experiments.

5.1.3.1 Sinusoidal distribution of the roughness

The cross sectional micro-/nano-profile of the upper silicon surface in the equivalent model (Figure 11) is described in equation (8):

$$\mathbf{f(x)} = \frac{\mathbf{L^2}}{\mathbf{2R\pi}}\mathbf{sin}^2\left(\frac{\pi x}{\lambda}\right),\ \mathbf{x \in (k\lambda - x_0; k\lambda + x_0)},\quad \mathbf{2x_0 \leq \lambda} \tag{8}$$

where k is an integer, x_0 is the length of the gap at the interface, R is the mean cap radius and λ is the periodic length of the gap. The maximum combined height of the gaps is given by equation (9):

$$\mathbf{h} = \frac{\lambda^2}{\mathbf{2R\pi}} \tag{9}$$

Based on to the contact mechanics of surfaces with periodic roughness, the pressure distribution below the asperity in the contact zone can be written as follows (10):

$$\mathbf{p(x)} = \frac{\cos(\frac{\pi x}{\lambda})}{\sqrt{\sin^2(\frac{\pi x_0}{\lambda}) - \sin^2(\frac{\pi x}{\lambda})}} \times \left\{\frac{E^*\lambda}{4\pi R}\left[\sin^2\left(\frac{\pi x_0}{\lambda}\right) - 2\sin^2\left(\frac{\pi x}{\lambda}\right)\right] + \frac{F}{\lambda}\right\} \tag{10}$$

where F is the total force exerted per asperity on the silicon surface by the adhesion force and the external force combined [30]. When k=0, we obtain:

$$\mathbf{p(x \to x_0^-)} = \frac{-K_I}{\sqrt{2\pi(x_0 - x)}} \tag{11}$$

$$\mathbf{K_I} = \left(\frac{E^*\lambda}{4\pi R}\sin^2\left(\frac{\pi x_0}{\lambda}\right) - \frac{F}{\lambda}\right).\sqrt{\lambda \cot(\frac{\pi x_0}{\lambda})} \tag{12}$$

where K_I is the stress intensity factor. If we neglect the surface force between the silicon surfaces in contact, the condition K_I=0 will be satisfied and we obtain:

$$\mathbf{F} = \frac{E^*\lambda^2}{4\pi R}\sin^2\left(\frac{\pi x_0}{\lambda}\right) \tag{13}$$

In the case of the surface profile given by f(x), the energy release rate in the gap outside the contact zone is given by:

$$\boldsymbol{\zeta} = \frac{\mathbf{K_I}^2}{\mathbf{2E^*}} \tag{14}$$

Based on JKR theory [31], the size of the contact zone $2x_o$ can be determined by taking ζ to be equal to the surface energy ω , which gives:

$$\mathbf{F_i} = \frac{\mathbf{E}^*\lambda^2}{\mathbf{4\pi R}} \mathbf{sin}^2\left(\frac{\mathbf{\pi x_{0_i}}}{\lambda}\right) - \sqrt{\mathbf{2E}^*\boldsymbol{\lambda}\boldsymbol{\omega}\,\mathbf{tan}\left(\frac{\mathbf{\pi x_{0_i}}}{\lambda}\right)} \tag{15}$$

The first term in this equation corresponds to the normalized Hertz pressure and the second one expresses the influence of the force exerted by the silicon surfaces on the contact zone [24, 30, 31].

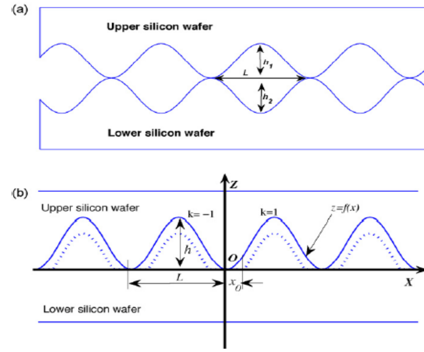

Figure 11: Schematic model for direct bonding between materials with periodically distributed asperities.

5.1.3.2 Gaussian distribution of the roughness

Function $\varphi(z) = \frac{1}{\sigma\sqrt{2\pi}} e^{(\frac{z^2}{2\sigma^2})}$ is the probability density required to express the Gaussian distribution of the height of the summits of the asperities (
Figure **12**). We assumed these asperities to be spherical and their radii R to be uniform. During the bonding process between the two surfaces under the external force P, the distance between the rigid surface and the average rough surface height is s. The number of asperities n in contact is given by (16) [30]:

$$\mathbf{n} = \mathbf{N}\int_{\mathbf{s}}^{\infty} \boldsymbol{\varphi}(\mathbf{z})\mathbf{dz} \tag{16}$$

If we focus on the ith asperity, the surface contact and the force can be written respectively:

$$\mathbf{A_i} = \boldsymbol{\pi}\mathbf{a_i^2} = \mathbf{R}\boldsymbol{\delta}_\mathbf{i} = \mathbf{R}(\mathbf{z_i} - \mathbf{s}) \tag{17}$$

$$\mathbf{F_i} = \mathbf{K}\sqrt{\mathbf{R}}\boldsymbol{\delta}_\mathbf{i}^{3/2} - \mathbf{2\pi\omega R} = \mathbf{K}\sqrt{\mathbf{R}}(\mathbf{z_i} - \mathbf{s})^{3/2} - \mathbf{2\pi\omega R} \tag{18}$$

From which the total contact surface and the total force can be deduced [24, 31-33]:

$$\mathbf{A} = \frac{\mathbf{NR}}{\sigma\sqrt{2\pi}}\int_{s}^{\infty}(\mathbf{z}-\mathbf{s})\,\mathbf{exp}\left(-\frac{\mathbf{z}^2}{2\sigma^2}\right)\mathbf{dz},\ \ \mathbf{F_{tot}} = \frac{\mathbf{NK}\sqrt{\mathbf{R}}}{\sigma\sqrt{2\pi}}\int_{s}^{\infty}(\mathbf{z_i}-\mathbf{s})^{3/2}\,\mathbf{exp}\left(-\frac{\mathbf{z}^2}{2\sigma^2}\right)\mathbf{dz} - \frac{\mathbf{2\pi\omega RN}}{\sigma\sqrt{2\pi}}\int_{s}^{\infty}\mathbf{exp}\left(-\frac{\mathbf{z}^2}{2\sigma^2}\right)\mathbf{dz} \quad (19)$$

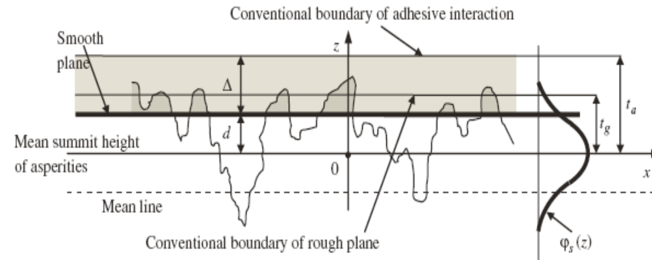

Figure 12: Gaussian distribution.

5.2 Modelling predictions

5.2.1 Finite element model

To compare the results obtained using the VCCT and cohesive element approaches, the results of razor blade tests were used. As shown in Figure 13, the sample selected for this purpose, which was composed of two silicon wafers bonded together, was 100 mm long (l), 40 mm wide (b) 2 mm thick (t). The main properties of the material were E=72.7 MPa, ν=0.16.
In order to use the VCCT approach, it is necessary to define an existing crack. The silicon glass blades were meshed using 8-node reduced integration brick elements (C3D8R).

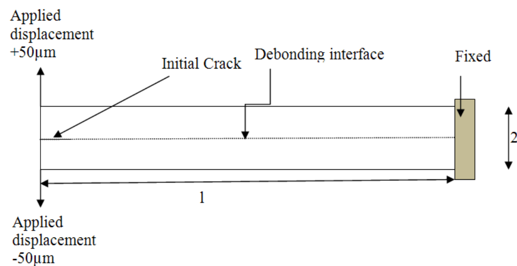

Figure 13: geometry of the razor blade specimen.

When the simulations were run with ABAQUS® cohesive elements, the geometry was the same as that shown in Figure 13. But in order to define the crack path, a layer of zero-thickness cohesive elements (COH4D8) was added corresponding to the dotted line shown in Figure 13.The glass blades were again meshed with C3D8R elements.

5.2.2 Parametric study for VCCT simulations

Simulations were performed with several mesh lengths and widths, taking several initial crack lengths and several values of the critical strain energy release rate (the other parameters of the power law criterion and are negligible when working solely in mode I) in order to determine the influence of these parameters. The modelling data obtained show that in the case of this imposed displacement, the crack expansion will not exceed 12mm (50 elements) or 11 mm (100 elements), and that the mesh width has no significant effects, whereas a slight decrease in the crack length will occur when the length of the elements decreases. The critical strain energy release rate was not found to have any significant effects (Table 3 and Figure14).

G_{IC} (J/m²)	Initial crack Lenght				
	2 mm	4 mm	6 mm	8 mm	10 mm
50x10x1					
10	10	8	6	4	2
100	10	8	6	4	2
50x20x1					
10	10	8	6	4	2
100	10	8	6	4	2
100x20x1					
10	8	7	5	3	1
100	8	7	5	3	1

Table 3: Crack expansion (in mm) calculated by performing VCCT simulations

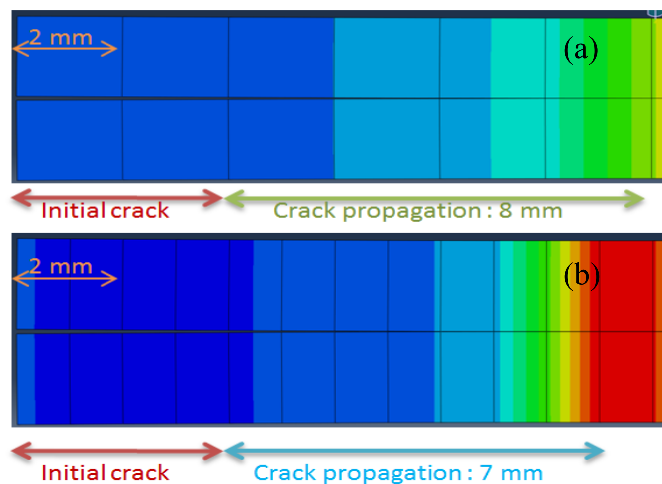

Figure 14: Crack extension with $G1_c$=100 J/m², initial crack length 2mm, (a) 50x10x1 mesh size and (b) 100x20x1 mesh size

5.2.3 Parametric study for cohesive element simulations

Simulations have to be performed with several mesh lengths and widths, with several values of the damage initiation parameters presented above, and with several critical strain energy release rates (the other parameters in the power law criteria and are negligible when working solely in mode I) in order to determine the influence of these parameters.

The results obtained are summarized in Table 4. In the case of this imposed displacement, the mesh size was found to slightly affect the crack length and the critical strain energy release rate . And as was to be expected, the data show that when the damage initiation parameters decrease, the crack length will increase.

G_{IC} (J/m²)	Damage initiation parameters (Mpa)		
	0,8	0,08	0,008
50x10x1			
10	6	8	14
100	6	8	14
100x10x1			
10	6	8	14
100	5	8	14
100x20x1			
10	6	8	14
100	5	8	14

Table 4: Crack extension (in mm) calculated by performing cohesive element simulations

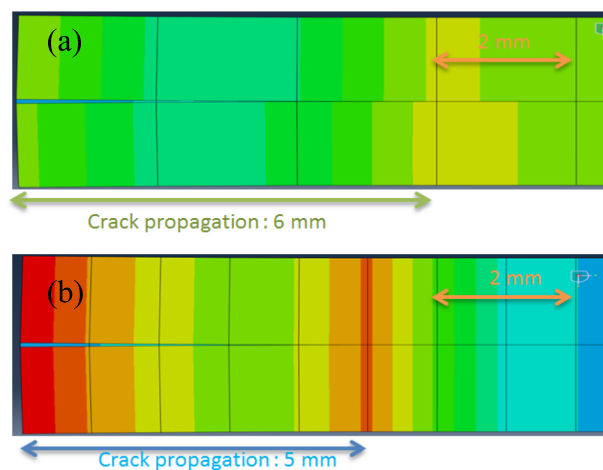

Figure 15: Crack extension for $G1_c$=100 J/m², damage initiation coefficient , (a) 50x10x1 mesh size and (b) 100x20x1 mesh size

6 Conclusion

In this paper, we investigated the direct bonding process. Chemical analysis of the surfaces to be bonded together showed that the bonding process was reversible, and the results of mechanical tests showed that thermal treatment increases the bonding energy at the bonded interface. Further mechanical tests (using the razor blade method) need to be performed in order to measure the interface energy. The results obtained in these initial modelling studies showed the influence of various modelling parameters such as the critical strain energy. However, other parametric studies need to be performed with these two models, and other simulations need to be carried out, using the integrated physical models for adhesion presented in Section 5, for example.

References

[1] Q.T. Tong, U. Gössele, “Semiconductor wafer bonding: recent developments”, Material Chemistry and Physics, 37, 101-107, 1994

[2] C. Gui, M. Elwenspoek, “The effect of surface roughness on direct wafer bonding”, Journal of Applied Physics, 85(10), 1999

[3] H. Nakanoshi and Al., “Studies on SIO2-SIO2 bonding with hydrofluoric acid. Room temperature and low stress binding technique for MEMS”, sensors and actuators A, 79, 237-244, 2000

[4] A. Berthold, MJ. Vellekoop, “ IC-compatible silicon wafer-to-wafer bonding”, sensors and actuators A, 60, 208-211, 1997

[5] O. Rayssac, « étude du collage par adhérence moléculaire hydrophile : application au contrôle de l’énergie de collage », University of Grenoble thesis, 1999

[6] A. Ploßl, G. Krauter, “Wafer direct bonding: Tailoring adhesion between brittle materials”, Materials Science and Engineering, 25, 1-88, 1999

[7] R. Stengl, T. Tan, O. Gössele, “a model for the silicon wafer bonding process”, Japanese Journal of Applied Physics, 28, 1735-1741, 1989

[8] F. Laurent, « étude et modélisation des performances de systèmes découpeurs d’images pour l’astronomie : application à l’instrumentation du JWST et du VLT », University of Saint-Etienne thesis, 2006

[9] C. Ventosa, F. Rieutord, “hydrophilic low temperature direct wafer bonding”, Journal of Applied Physics, 104, 123524, 2008

[10] C.Ventosa, C.Morales, “mechanism of thermal silicon oxide direct wafer bonding”, Electrochemical and Solid States Letters, 12, 375-379, 2009

[11] K. Gutjahr, T. Martini, U. Gössele, “Concept of wafer debonding”, Electrochemical Society Proceedings, 97(36), 72-74, 1998

[12] H.J. Bult and Al, “Physics and chemistry of surfaces”, Wiley, 2003

[13] www. kruss.de

[14] www.zygo.com/?/met/interferometers

[15] www.zygo.com/?/met/profilers

[16] H. Hamdane, Master report, university of Aix-Marseille 2010
[17] M. Raous, “Interfaces models coupling adhesion and friction”, Compte rendu mécaniques, 339, 491-501, 2011
[18] A. Ploßl, G. Krauter, “Wafer direct bonding: Tailoring adhesion between brittle materials”, Materials Science and Engineering, 25, 1-88, 1999
[19] Q.Y. Tong, U. Gosole, “Semiconductor wafer bonding: recent developments”, Materials Chemistry and physics, 17, 101-127, 1999
[20] O. Vallin et Al. , “Adhesion quantification methods for wafer bonding”, Materials Science and Engineering R ,50, 109-165, 2005
[21] Y. Bertholet et Al., “Steady-states measurement of wafer bonding cracking resistance”, Sensor and actuators A, 110, 157-163, 2004
[22] P. Gillis, J.J Gilman, “Double-cantilever cleavage mode of crack propagation”, Journal of Applied Physics, 35, 647-658, 1964
[23] W.P Maszara et Al., “Bonding of silicon wafers for silicon-on-insulator”, Journal of Applied Physics, 64(10), 4943-4950, 1988
[24] G. Liao et Al., “Effect of surface characteristic on room temperature silicon direct bonding”, Sensors and Actuators A, 158, 335-341, 2010
[25] C. Gui et Al., “The effect of surface roughness on direct wafer bonding”, Journal of applied physics, 85(10), 7448-7454, 1999
[26] V. Ranatunga, “Finite Element Modeling of Delamination crack propagation in laminated composites”, Proceedings of the world congress on Engineering 2011, vol III
[27] A. Leski, “Implementation of the virtual crack closure technique in engineering FR calculations”, Finite element in analysis and design 43, 261-268, 2007
[28] A.B. de Morais and al, “ Analysis of crack propagation in double cantilever beam test of multidirectional laminates”, mechanics of materials, 35, 641-652, 2003
[29] Dassault Systemes Simulia Corp., Abaqus Analysis User’s Manual, Providence, RI, 2011.
[30] Z. Tang et Al., “Modeling the formation of spontaneous wafer direct bonding under low temperature”, Microelectronic engineering, 85, 1754-1757, 2008
[31] K.L. Johnson, “The adhesion of two elastic bodies with slightly wavy surfaces”, International Journal of Solids and Structures, 32(¾), 423-430, 1995
[32] B.A. Galanov, “Models of adhesive contact between rough elastic solids”, International Journal of Mechanical Science, 2011
[33] G. Liao, X. Lin, “Surface roughness modeling for silicon direct bonding”, IEEE transaction on components, packaging and manufacturing technology, 1, 8, 2011

Appendix A: Samples characteristics

Materials	Diameter (mm)	Flatness (nm PTV)	Thickness (mm)	Roughness (nm RMS)
Zerodur	40.05	112	3.10	0.28
Zerodur	40.06	118	3.09	0.26
Silicon	40.08	145	3.10	0.26
Zerodur (debond)	40.06	81	3.10	0.25
Silicon (debond)	40.05	72	3.08	0.23

Table 5: Sample characteristics (wetting tests).

Samples	Materials	Diameter (mm)	Flatness (nm PTV)	Thickness (mm)	Roughness (nm RMS)
1-A-M-1	Zerodur	40.06	122	3.10	0.31
1-A-M-2	Zerodur	40.06	100	3.10	0.23
1-A-M-3	Silicon	40.05	76	3.10	0.33
1-A-M-4	Zerodur (debond)	40.06	80	3.10	0.26
1-A-M-5	Silicon (debond)	40.05	67	3.08	03

Table 6: Sample characteristics (XPS analysis).